Metasurface-Integrated Photonic Platform for Versatile Free-Space Beam Projection with Polarization Control

Alexander Yulaev,[1,2] Wenqi Zhu,[1,2] Cheng Zhang,[1,2] Daron A. Westly,[1] Henri J. Lezec,[1] Amit Agrawal,[1,2] and Vladimir Aksyuk[1,]*

[1]Physical Measurement Laboratory, National Institute of Standards and Technology, Gaithersburg, MD 20899, USA

[2]Maryland Nanocenter, University of Maryland, College Park, MD 20742, USA

Keywords: Integrated photonics, free-space radiation, metasurface, photonic-free-space coupling, polarization control, high-NA focusing

Abstract: Densely integrated photonic circuits enable scalable, complex processing of optical signals, including modulation, multiplexing, wavelength conversion, and detection. Directly interfacing such integrated circuits to free-space optical modes will enable novel optical functions, such as chip-scale sensing, interchip free-space interconnect and cooling, trapping, and interrogation of atoms. However, doing this within the limits of planar batch fabrication requires new approaches for bridging the large mode scale mismatch. Here, by integrating a dielectric metasurface with an extreme photonic mode converter, we create a versatile nanophotonic platform for efficient coupling to arbitrary-defined free-space radiation of 780 nm wavelength with well-controlled spatially-dependent polarization, phase, and intensity. Without leaving the chip, the high index photonic mode is converted first to a ≈ 200 μm wide, precisely collimated, linearly-polarized Gaussian beam, which is then modified by a planar, integrated, low-loss metasurface. We demonstrate high numerical aperture, diffraction limited focusing to an ≈ 473 nm spot at an ≈ 75 μm working distance, and combine it with simultaneous conversion from linear to elliptical polarization. All device components are lithographically defined and can be batch fabricated, facilitating future chip-scale low-cost hybrid photonic systems for bio-sensing, nonlinear signal processing and atomic quantum sensing, frequency references and memory.

Enabling integrated photonics circuits to send and receive arbitrary free-space optical beams and couple to objects in three-dimensional (3D) volumes brings compact, low-power, low-cost, versatile, and highly-scalable optical signals processing to applications traditionally done with bulky and costly free-space optics. Vice versa, this adds qualitatively new abilities to the photonics toolbox, such as free-space communication and optical measurement or integrated atomic quantum references[1-4] and sensors.[5-10] Particularly, atomic and molecular physics applications require millimeter and sub-millimeter scale optical fields for efficient optical cooling, or for suppression of room temperature transit time broadening, yet interaction strengths and detection quantum efficiency from individual trapped atoms and ions are maximized by diffraction-limited focusing with high numerical aperture. Often the atoms and ions must be kept far away from any walls and surfaces to minimize parasitic interactions. Due to the polarization-specific nature of light-matter interactions, constructing optical beams with an arbitrary-defined polarization is also key for engineering the desired interactions.[1, 2, 11]

However, such spatially-compact and efficient mode conversion between high-index photonic waveguides and wide free-space beams capable of long working distance propagation or high-numerical aperture (NA) focusing remains a challenge due to a large mode mismatch (> 10^5 times in modal area). Small-scale grating couplers efficiently bridge the mode mismatch between a sub-micrometer wide waveguide and typical optical fiber mode field diameters of 5 μm to 10 μm.[12-31] However, when scaled to larger sizes, such couplers fail to control light phase and intensity distribution sufficiently for accurate coupling directly to free-space modes that are hundreds of micrometers wide. Therefore, additional beam expansion volume is required and discrete optical components, such as micro-lenses, must be either accurately attached or 3D printed onto the photonic substrates, which adds significant fabrication costs, increases device size and restricts the application space. We have recently developed an entirely planar, microfabricated photonic extreme mode converter (EMC) capable of projecting a ≈ 200 μm wide collimated free-space Gaussian beam directly from a photonic circuit surface.[32, 33] While this development has bridged the mode mismatch gap and achieved accurate free-space intensity distribution and phase control, it was limited to creating linearly-polarized collimated Gaussian beams, lacking in spatial control of intensity, wavefront or polarization.

Planar optical metasurfaces (MS) made of judiciously arrayed, nanoscale elements have been recently developed to replace bulk optics such as optical lenses, waveplates, and prisms, providing a new versatile approach for arbitrary phase, amplitude, and polarization control.[34-47] A transmissive dielectric MS can convert a well-defined incident free-space beam into another free-space radiation mode enjoying engineered polarization, direction of propagation, and/or phase profile. Therefore, direct integration of such MS on the photonic EMC results in a compact, efficient and batch fabricated solution for versatile coupling between photonic circuitry and free-space. Here, we report a chip-scale planar nanophotonic platform made by integrating a photonic EMC with an optical metasurface for efficient coupling between a single-mode nanophotonic waveguide and free-space radiation with specified and well-controlled spatially-varying phase, intensity and polarization profiles, including high NA focusing, polarization state conversion, and grayscale intensity apodization and collimation. Using 780 nm light, we have demonstrated light focusing to a ≈ 473 nm full-width-at-half-maximum (FWHM) focal spot (NA ≈ 0.8) located ≈ 75 μm above the chip surface and polarization conversion to linear and elliptical states.

RESULTS AND DISCUSSION

Overall device structure and principle of operation, along with scanning electron microscope (SEM) images of the key components, are illustrated in Fig. 1. The waveguide to free-space mode conversion is based on three successive stages (Fig. 1a): (i) expansion of the waveguide mode into a wide collimated slab mode using spatially-variable evanescent coupling (Fig. 1b), (ii) free-space beam projection from the slab mode by a grating with spatially-variable period and duty cycle, and (iii) phase and polarization processing of the out-coupling light by a planar optical metasurface located directly above the chip grating (Fig. 1c). A red-color overlay in Fig. 1b depicts light propagation during the first two stages of expansion. Si_3N_4 is chosen as a broadband, low loss waveguide core material, clad in SiO_2 from top and bottom. The details of the first two stages of the photonic mode expansion have been previously reported.[46, 47] Briefly, the TE_0 waveguide mode is converted into an $\approx$ 200 μm FWHM collimated slab mode via evanescent coupling across the spatially-variable gap formed between the waveguide and the slab (Fig. 1b). The higher-effective-index slab wave propagates at an angle relative to the waveguide defined by phase-matching between the modes. By varying the gap size, the desired slab mode intensity distribution, such as a Gaussian beam, is obtained. The second stage of light expansion is realized by scattering the slab mode on an apodized grating, with dimensions optimized using a finite element method based inverse design procedure, projecting an $\approx$ 200 μm FWHM collimated 2D Gaussian beam propagating almost orthogonally to the chip surface (Fig. 1d). The beam polar angle and azimuthal direction are controlled by the grating period design, as well as by rotating the grating slightly relative to the incident slab mode. The slab mode is transverse-electric (TE) polarized, and the free-space beam remains linearly polarized with electric-field projection parallel to the grating lines. In the final stage, the collimated two-dimensional (2D) Gaussian beam interacts with a metasurface made of an array of Si nanopillars. Here, a low-loss dielectric metasurface, operating in transmission, flexibly processes light phase and polarization to obtain very general spatially-dependent wavefront and polarization transformations. Such MS designs can be implemented in our platform without limitation, as required by specific applications. We have tested two different devices with metasurfaces designed to perform the two key functions: (1) shaping the wavefront, demonstrated by high-NA focusing and tilt correction to surface-normal (as illustrated in Fig. 1d) and (2) polarization transformation demonstrated by implementing a wave-plate converting polarization from linear to elliptical.

In the first device, the tilting and focusing metasurface is built using polarization-independent square-cross-section elements, with the local element width and pitch defining the phase added to the transmitted light according to:

$$\varphi = \mathrm{mod}\{\left(k_0\left(f - \sqrt{x^2 + y^2 + f^2}\right) - k_0 x \sin\theta_{comp}\right), 2\pi\}, \tag{1}$$

Here, k_0 and f stand for the free-space wave number and the MS focal distance, respectively, and θ_{comp} is the polar angle of the collimated beam emanated from the photonic grating into free space when the MS is not present. In this case, we specify that the focused beam be axially symmetric around the surface normal, therefore a tilt-angle-compensating linear phase is subtracted, akin to a bulk optical wedge.

In the second device, the metasurface consists of an array of rectangular cross-section elements, each oriented at 45° relative to the linear polarization of the incident wide collimated beam projected by the EMC. The incident radiation couples to both orthogonally-polarized modes of the rectangular MS element, propagating with different effective indexes through the MS, resulting in a phase shift between the two polarizations after propagation. Choosing specific dimensions of MS elements, we can spatially vary both the common and the relative phase shifts of polarization components, shaping the output wavefront and polarization state simultaneously.

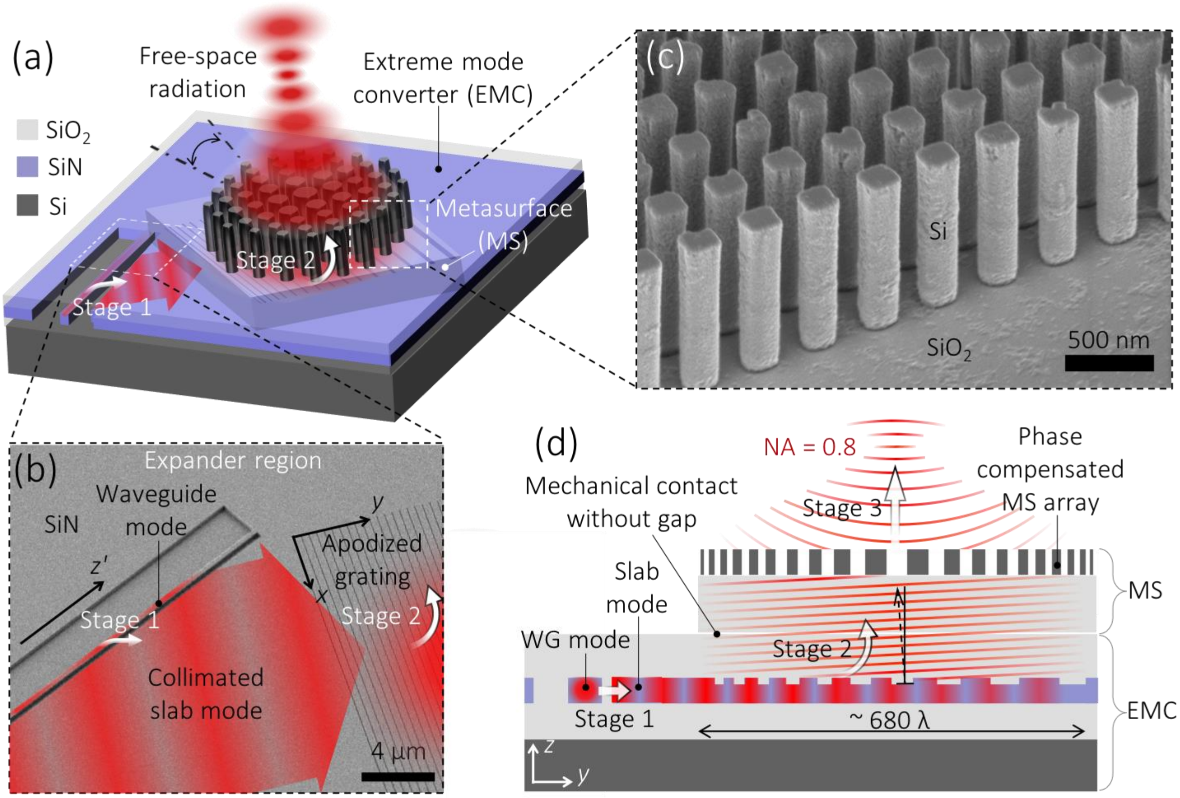

Figure 1. Metasurface-integrated photonic platform is illustrated using high-NA focusing as an example. (a) A schematic illustrating the device structure and operation: stage 1 – an expansion of the waveguide mode to a collimated 1D Gaussian slab mode, stage 2 – slab mode scattering by an apodized grating into free space forming a collimated 2D Gaussian beam, stage 3 – light focusing using a planar MS located directly above the grating. (b) An SEM image showing parts of the evanescent expander (stage 1) and apodized grating (stage 2). Red color overlay depicts a waveguide mode expanding into a collimated slab mode followed by scattering into free space by an apodized grating (stage 2). (c) An SEM image of a portion of the MS showing an array of Si pillars fabricated on a SiO_2 substrate. (d) A cross-sectional schematic, depicting a wide collimated beam emanated at a slight angle from the chip normal and subsequently tilted to normal and focused by the MS with NA $\approx$ 0.8.

While monolithic wafer-scale nanofabrication of the metasurface directly on the EMC is straightforward, here for expediency and flexibility, a photonic EMC and MS are fabricated separately and then assembled into a single photonic platform as illustrated in the flow chart in Fig. 2. The details of device fabrication are specified in the Method section. Briefly, the EMC device is made via depositing continuous layers of SiO_2 bottom layer and SiN followed by photonic structure patterning using electron beam lithography (EBL) and reactive ion etching (RIE). The chip is then clad into SiO_2. The MS part is fabricated on a fused silica substrate by depositing Si layer followed by patterning using EBL and inductively-coupled plasma RIE. The MS chip is brought in contact with the converter chip and manually aligned relative to it under a microscope by in-plane rotation and translation.

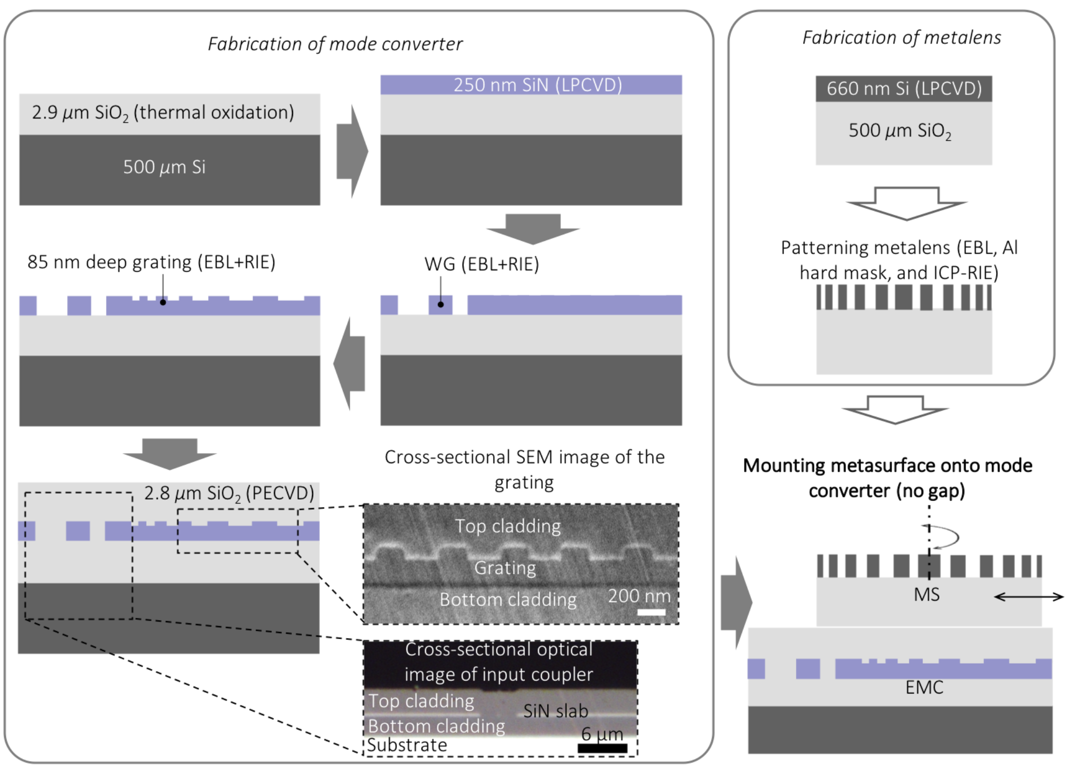

Figure 2. Device fabrication sequence. For convenience, planar EMC and MS are fabricated separately and then assembled into the single photonic platform. Cross-sectional SEM and optical

images show the fine structures of Si_3N_4 grating and evanescent expander clad in SiO_2 from top and bottom, respectively.

Our photonic platform function is reciprocal and can be used to couple free-space light into a single-mode waveguide, as well as producing a desired free-space mode from the waveguide mode. In the experimental apparatus, shown in Fig. 3a, we use a fiber-coupled laser source to feed the photonic platform and an optical microscope to characterize the free-space output radiation. 780 nm wavelength laser radiation is coupled from a regular single-mode optical fiber to the TE_0 waveguide mode via inverted-taper waveguide couplers fabricated on a photonic chip's edge. The input polarization and power (typically $\approx$ 1 mW) are adjusted by a manual fiber polarization controller and an attenuator, respectively. Characterization of free-space radiation is performed using an optical microscope equipped with 10× and 100× objectives and a charge coupled device (CCD) camera mounted above the chip surface. The experimental procedures follow the three successive steps illustrated in dashed boxes in Fig. 3a: (i) free-space beam characterization using 10× objective (NA = 0.3) to confirm collimation and quantify the beam tilt, (ii) MS alignment on an EMC, and (iii) MS focal spot characterization using 100× objective (NA = 0.9).

To analyze the free-space beam projected from the EMC photonic chip, optical images of the output light have been acquired at 0 mm, 1.85 mm, 3 mm, and 5.7 mm above the chip surface. Images captured at 0 mm (left) and 5.7 mm (right) are shown in Fig. 3b. The shape of the beam is Gaussian with an average FWHM equal to 195 μm ± 20 μm, and no statistically significant width change is observed, indicating good collimation (Fig. S1). The reported uncertainty of FWHM is the standard deviation value obtained from five independently measured beam images, which are fit with two-dimensional Gaussian profiles. The shift in the beam center yields a polar angle $\theta =$

$5.2^{o} \pm 0.1^{o}$, consistent with the EMC design and used to select the proper tilt angle compensation for the MS pattern to focus without optical aberrations and emanate the output light beam orthogonally to the surface (Fig. S2). The reported polar angle uncertainty corresponds to one standard deviation statistical uncertainty obtained from analyzing Gaussian-fit beam shifts as a function of height *z*.

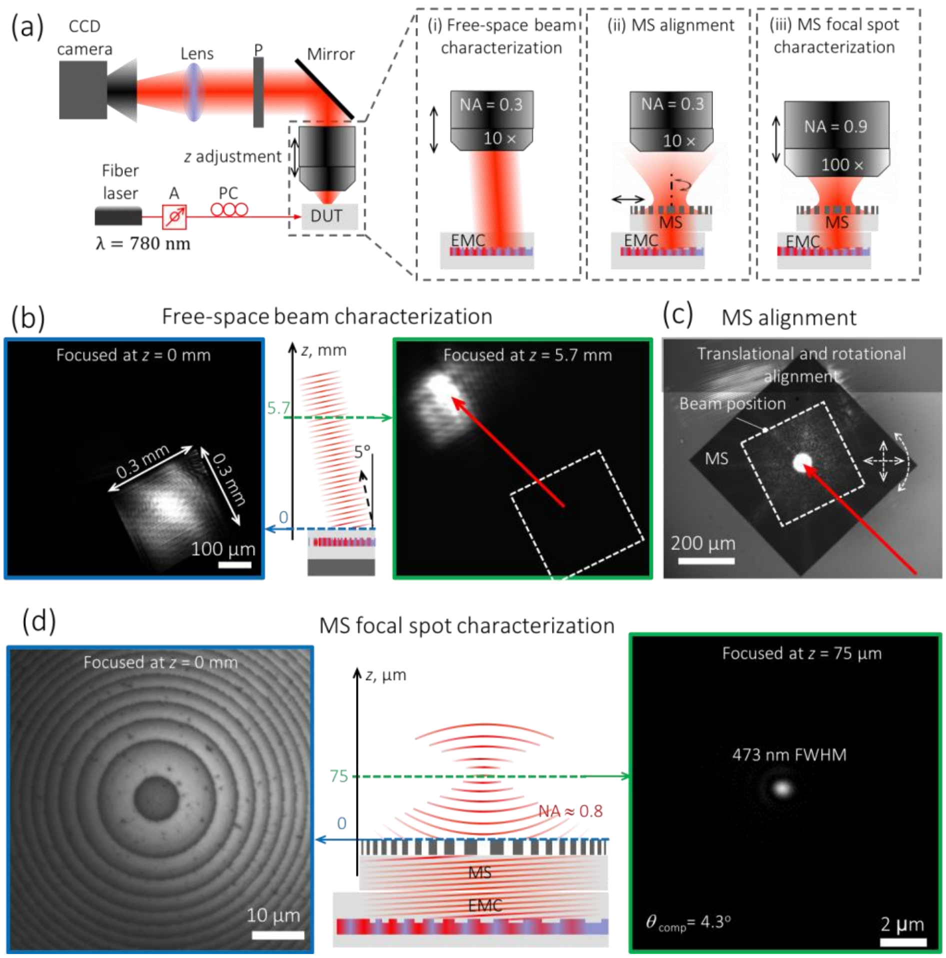

Figure 3. Experimental characterization of device operation. (a) An experimental set-up: A is a fiber attenuator, PC is a manual fiber polarization controller, DUT is a device under test, P is a polarizer. Dashed boxes illustrate three assemblies to (i) characterize a free-space beam projected by an EMC, (ii) align MS on top of the EMC, and (iii) analyze overall device operation including focal spot characterization. (b) Free-space beam characterization: two optical images of the light beam projected from the photonic EMC into free space acquired at 0 mm (left) and 5.7 mm (right)

above the chip surface. The dashed box indicates the position of the EMC beam at the MS surface, i.e. z = 0 mm. (c) MS alignment: a phase-compensated MS is mounted and aligned on the EMC chip. The image is captured using a 10× objective. The dashed box indicates the position of the light beam. The red arrow in panels (b) and (c) indicate the in-plane projection of the collimated free-space beam, which is aligned to be collinear with the phase compensation direction incorporated into the MS design. (d) MS focal spot characterization: two optical images obtained at 0 μm (left) and 75 μm (right) above the device surface using NA=0.9, 100× objective depict the MS surface structure under white light illumination and the device-generated focal spot with 780 nm light, respectively. The aberration-free focal spot with the FWHM ≈ 473 nm appears ≈ 75 μm above the chip surface.

After EMC characterization, a nominally 4.3°-tilt-compensating MS and the EMC chip are brought into a direct mechanical contact, and MS is manually shifted and rotated to align to the EMC under the low NA 10× microscope (Fig. 3c). The compensation direction of the MS, along one of its edges, is rotationally aligned along the azimuthal direction of the beam tilt (red arrows), while the MS is centered on the EMC output beam. We first characterize the device performance with a MS focusing light with a high NA. Once the MS is aligned on a chip, 100× objective with NA = 0.9 is employed to characterize light focusing. Two optical micrographs, with image planes at 0 μm and 75 μm above the device surface (Fig. 3d), show the MS fine structure under white light illumination, and the 780 nm wavelength focal spot, respectively. Within a couple degrees of rotational misalignment between the MS and EMC estimated, the focal spot image appears axially symmetric, with no apparent aberrations or additional features (Fig. 3d, right and Fig. S3). The measured 75 μm ± 2.5 μm focal distance from MS surface is in agreement with the simulated value of 72.7 μm (Fig. S4). The uncertainty of the focal distance is half of the smallest scale division of the z-stage manual positioner. The details of the focal spot analysis are shown in Fig. S5.

The coupling efficiency of a TE waveguide mode to a collimated beam is ≈ 4.5 dB, and the focusing efficiency of the MS results in ≈ 1.9 dB, yielding 6.4 dB overall efficiency of the photonic platform. The device's bandwidth is limited by 780 nm ± 4 nm, ensuring an aberration-free diffraction limited focal spot. The bandwidth of the EMC spans tens of nanometers, however the beam steering effect leads to a variation of the incident angle at the tilt-compensated MS, and beyond the specified range, comma aberrations are observed.

Fitting the CCD image data by an axially symmetric 2D Gaussian function, yields FWHM = 473 nm ± 71 nm. Here we estimate the uncertainty due to the mismatch between the data and the Gaussian model by separately fitting a 2D Gaussian with unequal width along the principal axes and reporting the width difference as the uncertainty. The statistical uncertainty of the width from the fit is negligible compared to this width mismatch along orthogonal axes. Changing the MS rotation angle by an estimated ≈ 4° gives a similar tight focal spot with Gaussian intensity FWHM = 480 nm ± 35 nm. Note that these values describe the focal spot image size on the CCD without any attempt to remove the effects of potentially imperfect imaging by the 100×, NA = 0.9 objective. The measured value is consistent with an Airy FWHM ≈ 0.5 λ/NA = 487.5 nm for NA = 0.8 and the numerically simulated value of ≈ 478 nm.

Finally, we demonstrate the capability of our platform to arbitrarily control light polarization, when the EMC is integrated with a MS operating as both a wave plate and a metalens. As a demonstration, we obtain an elliptically polarized light focused in free-space using the MS made of rectangular cross-section elements. To characterize the MS effect on polarization, we insert a linear polarizer in the imaging optical path after the microscope objective and capture and analyze series of images with different polarizer orientations. We first capture a series of low magnification images containing both the polarization-modified light beam processed by the MS and a pristine linear polarized reference light beam coming from an adjacent identical EMC using the 10× objective (NA = 0.3) (Fig. 4a). The reference EMC 2 is located close to the initial EMC 1 but rotated 180° relative to it. Fabricating and using two identical EMCs close to each other makes it possible to observe both beams simultaneously, spatially separated but within the same field of view and use one of them as a reference device. The dependence of the spatially-integrated light intensity of both beams on polarizer orientation (Fig. 4b) reveals the elliptical polarization state of the MS-processed radiation indicated by the reduction of the polarization contrast visibility from ≈ 1 (linearly polarized reference) to 0.46 ± 0.02 (elliptically polarized after the MS). The small ≈ 8° relative shift between the two curves confirms rotational misalignment of less than 5° between the MS and the EMC.

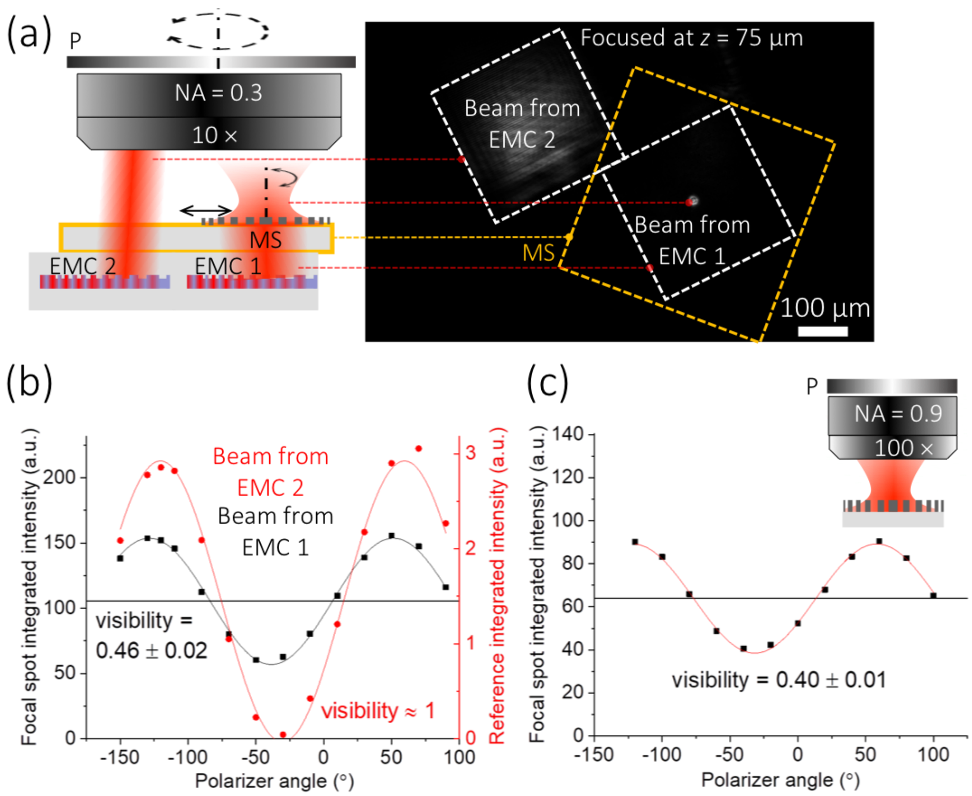

Figure 4. Characterizing the polarization state of the output beam projected from the photonic platform. (a) An experiment schematic and an optical image (10×, NA = 0.3) simultaneously

capturing the elliptically-polarized focused light beam after the MS illuminated by the EMC 1 and a linearly-polarized, collimated reference beam coming from an identical, 180° rotated EMC 2 without a MS. The focal plane is detuned from best focus to avoid camera saturation. (b) The dependence of integrated light intensity of both linearly-polarized reference (red curve) and elliptically-polarized MS (black curve) beams on polarizer orientation. The analysis is based on a series of images, as in panel (a), captured with different polarizer orientations. (c) The dependence of integrated light intensity of the elliptically-polarized focal spot captured by 100× objective (NA = 0.9) on polarizer orientation. Here, similar visibility is obtained with light captured over the full numerical aperture of the device.

While the 10× objective only captures light from the center portion of the lens due to the objective's limited NA, switching to a 100× objective (NA = 0.9) allows us to fully capture the light passing through the MS focus (however without the ability to simultaneously image the reference, which falls outside of the objective's field of view). Performing the same analysis – intensity vs. polarizer orientation – results in the similar visibility 0.40 ± 0.01 (Fig. 4c) as the one obtained using a low-NA objective, indicating that the polarization transformation is performed uniformly across the MS. The uncertainty in both cases is one standard deviation statistical uncertainty of the visibility, i.e. sinusoidal fit amplitude normalized by the offset.

Precise lithographic definition and the ability to scale photonics to thousands of individual signals provides an unprecedented opportunity for future scalable and low-cost free-space optical applications using multiple precisely-aligned collimated beams, focused spots, Bessel beams and light sheets, and other free-space optical modes at multiple wavelengths, all created by batch-fabricated photonic chips. For example, resilient to local perturbations, Bessel beams allow tight focusing at long working distances, useful for structured illumination in fluorescence microscopy.[48-50] The presented efficient photonic to free-space coupling is reciprocal, enabling highly-selective radiation collection, filtering, processing and detection on chip. EMC has been experimentally demonstrated for both free-space illumination and single-mode collection into a waveguide,[32] and combining it with MS permits selective high-NA collection of radiation with the desired polarization, such as circular,[34, 35] required for some atom applications. Advances in robust, efficient and manufacturable integration of photonics with free-space matter, such as atoms and their ensembles in a vacuum or in a solid-state matrix, can add electric[51] and magnetic[52] field sensing, accurate wavelengths references,[2] as well as, potentially, strong photon-photon interactions and optical memory, to the photonics technology. Other applications that stand to benefit from this technology are high density interconnect for fiber-optic communication, miniaturized systems for light detection and ranging (LIDAR) as well as on-chip chemical and biological detection. Finally, the capabilities of the proposed platform can be readily extended by integrating the EMC with reconfigurable/tunable MSs, where the tuning mechanism is realized using mechanical, chemical, optical or thermal switching.

CONCLUSION

To conclude, we have realized a compact metasurface-integrated photonic platform enabling conversion between a sub-micrometer photonic guided mode and the desired free-space radiation field profiles including well-controlled light focusing, polarization, and lateral intensity distribution. Functionality is demonstrated by diffraction-limited aberration-free focusing in the far field $\approx$ 75 μm ($\approx$ 100 λ) above the chip surface with high numerical aperture (NA = 0.8) producing a focal spot with $\approx$ 473 nm FWHM. Conversion of the polarization state from linear to elliptical is shown simultaneously with focusing. While the hybrid integration approach permits flexible mix-and-match between known good MS and photonic mode converter components, the microfabrication materials and processes are conventional and mutually-compatible, permitting straightforward wafer-scale monolithic batch fabrication of such integrated planar photonic devices. Multiple identical or different optical devices can be simultaneously fabricated and accurately arranged on the same chip and interconnected by custom nanophotonic circuitry for specific applications. This approach in principle allows creation of wide beams with arbitrary spatially-varying wavefronts and polarizations directly from the planar photonic device surface, and can be easily adapted for infrared, ultraviolet, and visible ranges. Both the metasurface and the mode converter are non-resonant, wide-bandwidth devices, and the dispersion of the mode converter grating can be used for active beam steering based on optical frequency tuning. The developed photonic platform paves the way for integrated chip-scale quantum atomic-photonic devices, novel integrated nonlinear photonics, and chip-scale optical sensors for chemical and biological detection.

METHODS

Fabrication of the photonic chip: Fabrication of the EMC starts from 100 mm diameter Si wafer, which undergoes thermal oxidation resulting in ≈ 2.9 μm thick oxide. Then a continuous ≈ 250 nm thick layer of Si_3N_4 is deposited using low pressure chemical vapor deposition (LPCVD) followed by a two-stage patterning. Electron beam lithography (EBL) and reactive ion etching (RIE) are employed to define nominally 300 nm wide waveguides, expander region with an adiabatically varying gap, and inverse tapers served to couple light from fiber array to the photonic device. During the second run of EBL and RIE, ≈ 85 nm deep groves are made, forming an apodized grating. To complete the first component of the platform, ≈ 2.8 μm thick SiO_2 is clad conformally using plasma-enhanced chemical vapor deposition (PECVD). The wafer then is diced into separate chips, and facets with input couplers are polished. The shape and dimensions of critical photonic elements such as an evanescent coupler and an apodized grating (see inset images in Fig. 2) are checked using SEM imaging before SiO_2 cladding deposition.

Fabrication of the MS: To fabricate the MS part of the device, a layer of nominally 660 nm thick polycrystalline silicon is deposited onto a fused silica wafer via LPCVD. Then the MS fine structure is patterned using EBL and inductively-coupled-plasma reactive ion etching (ICP-RIE) through an Al hard mask to form standing Si nanowires with a high aspect ratio. Finally, the Al hard mask is removed using a wet etchant.

ASSOCIATED CONTENT

Supporting information. Characterization of a wide collimated free-space beam and MS processed focal spot. Quantifying effects of phase compensation and rotational misalignment on focal spot aberration. Simulations of the light intensity distribution of a phase-corrected metasurface and the E-field and time-delay of polarization-conversion metasurface.

The following files are available free of charge.
Supporting information (DOC)

AUTHOR INFORMATION

Corresponding Author
*E-mail: vladimir.aksyuk@nist.gov

Author Contributions
The manuscript was written through contributions of all authors. All authors have given approval to the final version of the manuscript.

Notes

The authors declare no competing financial interest.

ACKNOWLEDGEMENTS

Drs. Alexander Yulaev, Wenqi Zhu, Cheng Zhang, and Amit Agrawal acknowledge support under the Cooperative Research Agreement between the University of Maryland and the National Institute of Standards and Technology Center for Nanoscale Science and Technology, Award 70NANB10H193, through the University of Maryland.

REFERENCES

1. Kitching, J.; Donley, E. A.; Knappe, S.; Hummon, M.; Dellis, A.; Sherman, J.; Srinivasan, K.; Aksyuk, V. A.; Li, Q.; Westly, D. In *NIST on a Chip: Realizing SI units with microfabricated alkali vapour cells*, Journal of Physics: Conference Series, 2016; IOP Publishing: 012056.

2. Hummon, M. T.; Kang, S.; Bopp, D. G.; Li, Q.; Westly, D. A.; Kim, S.; Fredrick, C.; Diddams, S. A.; Srinivasan, K.; Aksyuk, V.; Kitching, J.E. Photonic chip for laser stabilization to an atomic vapor with 10− 11 instability. *Optica* **2018,** *5*, 443-449.

3. Mehta, K. K.; Bruzewicz, C. D.; McConnell, R.; Ram, R. J.; Sage, J. M.; Chiaverini, J. Integrated optical addressing of an ion qubit. *Nature nanotechnology* **2016,** *11*, 1066-1070.

4. Kohnen, M.; Succo, M.; Petrov, P.; Nyman, R.; Trupke, M.; Hinds, E. An array of integrated atom–photon junctions. *Nature Photonics* **2011,** *5*, 35-38.

5. Xu, D.-X.; Densmore, A.; Delâge, A.; Waldron, P.; McKinnon, R.; Janz, S.; Lapointe, J.; Lopinski, G.; Mischki, T.; Post, E. Folded cavity SOI microring sensors for high sensitivity and real time measurement of biomolecular binding. *Optics express* **2008,** *16*, 15137-15148.

6. Lin, S.; Crozier, K. B. Trapping-assisted sensing of particles and proteins using on-chip optical microcavities. *ACS nano* **2013,** *7*, 1725-1730.

7. Sun, Y.; Fan, X. Optical ring resonators for biochemical and chemical sensing. *Analytical and bioanalytical chemistry* **2011,** *399*, 205-211.

8. Squires, T. M.; Messinger, R. J.; Manalis, S. R. Making it stick: convection, reaction and diffusion in surface-based biosensors. *Nature biotechnology* **2008,** *26*, 417-426.

9. Dantham, V.; Holler, S.; Kolchenko, V.; Wan, Z.; Arnold, S. Taking whispering gallery-mode single virus detection and sizing to the limit. *Applied Physics Letters* **2012,** *101*, 043704.

10. Zhu, J.; Ozdemir, S. K.; Xiao, Y.-F.; Li, L.; He, L.; Chen, D.-R.; Yang, L. On-chip single nanoparticle detection and sizing by mode splitting in an ultrahigh-Q microresonator. *Nature photonics* **2010,** *4*, 46-49.
11. Grier, D. G. A revolution in optical manipulation. *Nature* **2003,** *424*, 810-816.
12. Dakss, M.; Kuhn, L.; Heidrich, P.; Scott, B. Grating coupler for efficient excitation of optical guided waves in thin films. *Applied physics letters* **1970,** *16*, 523-525.
13. Harris, J.; Winn, R.; Dalgoutte, D. Theory and design of periodic couplers. *Applied Optics* **1972,** *11*, 2234-2241.
14. Vedantam, S.; Lee, H.; Tang, J., Conway, J.; Staffaroni, M.; Yablonovitch, E., A plasmonic dimple lens for nanoscale focusing of light. *Nano letters* **2009**, *9*, 3447-3452.
15. Yariv, A.; Yeh, P. Photonics: optical electronics in modern communications (the oxford series in electrical and computer engineering). *Oxford University Press, Inc* **2006,** *231*, 232.
16. Xiao, T.P.; Cifci, O.S.; Bhargava, S.; Chen, H.; Gissibl, T.; Zhou, W.; Giessen, H.; Toussaint Jr, K.C.; Yablonovitch, E.; Braun, P.V. Diffractive spectral-splitting optical element designed by adjoint-based electromagnetic optimization and fabricated by femtosecond 3D direct laser writing. *ACS Photonics* **2016,** *3*, 886-894.
17. Ogawa, K.; Chang, W.; Sopori, B.; Rosenbaum, F. A theoretical analysis of etched grating couplers for integrated optics. *IEEE Journal of Quantum Electronics* **1973,** *9*, 29-42.
18. Taillaert, D.; Bienstman, P.; Baets, R. Compact efficient broadband grating coupler for silicon-on-insulator waveguides. *Optics letters* **2004,** *29*, 2749-2751.
19. Van Laere, F.; Roelkens, G.; Ayre, M.; Schrauwen, J.; Taillaert, D.; Van Thourhout, D.; Krauss, T. F.; Baets, R. Compact and highly efficient grating couplers between optical fiber and nanophotonic waveguides. *Journal of lightwave technology* **2007,** *25*, 151-156.
20. Ding, Y.; Peucheret, C.; Ou, H.; Yvind, K. Fully etched apodized grating coupler on the SOI platform with− 0.58 dB coupling efficiency. *Optics letters* **2014,** *39*, 5348-5350.
21. Roelkens, G.; Vermeulen, D.; Van Thourhout, D.; Baets, R.; Brision, S.; Lyan, P.; Gautier, P.; Fedeli, J.-M. High efficiency diffractive grating couplers for interfacing a single mode optical fiber with a nanophotonic silicon-on-insulator waveguide circuit. *Applied Physics Letters* **2008,** *92*, 131101.
22. Vermeulen, D.; Selvaraja, S.; Verheyen, P.; Lepage, G.; Bogaerts, W.; Absil, P.; Van Thourhout, D.; Roelkens, G. High-efficiency fiber-to-chip grating couplers realized using an advanced CMOS-compatible silicon-on-insulator platform. *Optics express* **2010,** *18*, 18278-18283.
23. Ding, Y.; Ou, H.; Peucheret, C. Ultrahigh-efficiency apodized grating coupler using fully etched photonic crystals. *Optics letters* **2013,** *38*, 2732-2734.
24. Zaoui, W. S.; Kunze, A.; Vogel, W.; Berroth, M.; Butschke, J.; Letzkus, F.; Burghartz, J. Bridging the gap between optical fibers and silicon photonic integrated circuits. *Optics express* **2014,** *22*, 1277-1286.

25. Chen, X.; Li, C.; Fung, C. K.; Lo, S. M.; Tsang, H. K. Apodized waveguide grating couplers for efficient coupling to optical fibers. *IEEE Photonics Technology Letters* **2010,** *22,* 1156-1158.

26. Mehta, K. K.; Ram, R. J. Precise and diffraction-limited waveguide-to-free-space focusing gratings. *Scientific reports* **2017,** *7,* 2019.

27. Mekis, A.; Gloeckner, S.; Masini, G.; Narasimha, A.; Pinguet, T.; Sahni, S.; De Dobbelaere, P. A grating-coupler-enabled CMOS photonics platform. *IEEE Journal of Selected Topics in Quantum Electronics* **2011,** *17,* 597-608.

28. Xu, X.; Subbaraman, H.; Covey, J.; Kwong, D.; Hosseini, A.; Chen, R. T. Complementary metal–oxide–semiconductor compatible high efficiency subwavelength grating couplers for silicon integrated photonics. *Applied Physics Letters* **2012,** *101,* 031109.

29. Song, J. H.; Doany, F. E.; Medhin, A. K.; Dupuis, N.; Lee, B. G.; Libsch, F. R. Polarization-independent nonuniform grating couplers on silicon-on-insulator. *Optics letters* **2015,** *40,* 3941-3944.

30. Chen, X.; Xu, K.; Cheng, Z.; Fung, C. K.; Tsang, H. K. Wideband subwavelength gratings for coupling between silicon-on-insulator waveguides and optical fibers. *Optics letters* **2012,** *37,* 3483-3485.

31. Halir, R.; Cheben, P.; Schmid, J.; Ma, R.; Bedard, D.; Janz, S.; Xu, D.-X.; Densmore, A.; Lapointe, J.; Molina-Fernández, I. Continuously apodized fiber-to-chip surface grating coupler with refractive index engineered subwavelength structure. *Optics letters* **2010,** *35,* 3243-3245.

32. Kim, S.; Westly, D. A.; Roxworthy, B. J.; Li, Q.; Yulaev, A.; Srinivasan, K.; Aksyuk, V. A. Photonic waveguide to free-space Gaussian beam extreme mode converter. *Light: Science & Applications* **2018,** *7,* 72.

33. Yulaev, A.; Kim, S.; Westly, D. A.; Roxworthy, B. J.; Li, Q.; Srinivasan, K. A.; Aksyuk, V. A. In *Collimating a Free-Space Gaussian Beam by Means of a Chip-Scale Photonic Extreme Mode Converter*, 2018 International Conference on Optical MEMS and Nanophotonics (OMN), 2018; IEEE: 1-2.

34. Kildishev, A. V.; Boltasseva, A.; Shalaev, V. M. Planar photonics with metasurfaces. *Science* **2013,** *339,* 1232009.

35. Yu, N.; Capasso, F. Flat optics with designer metasurfaces. *Nature materials* **2014,** *13,* 139-150.

36. Yu, N.; Genevet, P.; Kats, M. A.; Aieta, F.; Tetienne, J.-P.; Capasso, F.; Gaburro, Z. Light propagation with phase discontinuities: generalized laws of reflection and refraction. *Science* **2011,** *334,* 333-337.

37. Lin, D.; Fan, P.; Hasman, E.; Brongersma, M. L. Dielectric gradient metasurface optical elements. *Science* **2014,** *345,* 298-302.

38. Lin, J.; Genevet, P.; Kats, M. A.; Antoniou, N.; Capasso, F. Nanostructured holograms for broadband manipulation of vector beams. *Nano letters* **2013,** *13,* 4269-4274.

39. Shi, Z.; Khorasaninejad, M.; Huang, Y.-W.; Roques-Carmes, C.; Zhu, A. Y.; Chen, W. T.; Sanjeev, V.; Ding, Z.-W.; Tamagnone, M.; Chaudhary, K.; Devlin, R. C.; Qiu, C.-W.; Capasso, F. Single-layer metasurface with controllable multiwavelength functions. *Nano letters* **2018,** *18*, 2420-2427.

40. Khorasaninejad, M.; Aieta, F.; Kanhaiya, P.; Kats, M. A.; Genevet, P.; Rousso, D.; Capasso, F. Achromatic metasurface lens at telecommunication wavelengths. *Nano letters* **2015,** *15*, 5358-5362.

41. Aieta, F.; Genevet, P.; Kats, M. A.; Yu, N.; Blanchard, R.; Gaburro, Z.; Capasso, F. Aberration-free ultrathin flat lenses and axicons at telecom wavelengths based on plasmonic metasurfaces. *Nano letters* **2012,** *12*, 4932-4936.

42. Arbabi, A.; Horie, Y.; Bagheri, M.; Faraon, A. Dielectric metasurfaces for complete control of phase and polarization with subwavelength spatial resolution and high transmission. *Nature nanotechnology* **2015,** *10*, 937-943.

43. Khorasaninejad, M.; Chen, W. T.; Devlin, R. C.; Oh, J.; Zhu, A. Y.; Capasso, F. Metalenses at visible wavelengths: Diffraction-limited focusing and subwavelength resolution imaging. *Science* **2016,** *352*, 1190-1194.

44. Chen, H.-T.; Taylor, A. J.; Yu, N. A review of metasurfaces: physics and applications. *Reports on progress in physics* **2016,** *79*, 076401.

45. Kamali, S. M.; Arbabi, E.; Arbabi, A.; Faraon, A. A review of dielectric optical metasurfaces for wavefront control. *Nanophotonics* **2018,** *7*, 1041-1068.

46. Khorasaninejad, M.; Capasso, F. Metalenses: Versatile multifunctional photonic components. *Science* **2017,** *358*, eaam8100.

47. Maguid, E.; Yulevich, I.; Yannai, M.; Kleiner, V.; Brongersma, M. L.; Hasman, E. Multifunctional interleaved geometric-phase dielectric metasurfaces. *Light: Science & Applications* **2017,** *6*, e17027.

48. Mertz, J. Optical sectioning microscopy with planar or structured illumination. *Nature methods* **2011,** *8*, 811-819.

49. Gao, L.; Shao, L.; Chen, B.-C.; Betzig, E. 3D live fluorescence imaging of cellular dynamics using Bessel beam plane illumination microscopy. *Nature protocols* **2014,** *9*, 1083-1101.

50. Planchon, T. A.; Gao, L.; Milkie, D. E.; Davidson, M. W.; Galbraith, J. A.; Galbraith, C. G.; Betzig, E. Rapid three-dimensional isotropic imaging of living cells using Bessel beam plane illumination. *Nature methods* **2011,** *8*, 417-423.

51. Holloway, C.; Simons, M.; Gordon, J.; Wilson, P.; Cooke, C.; Anderson, D.; Raithel, G. Atom-Based RF Electric Field Metrology: From Self-Calibrated Measurements to Subwavelength and Near-Field Imaging. *IEEE Transactions on Electromagnetic Compatibility* **2017,** *59*, 717-728.

52. Shah, V.; Knappe, S.; Schwindt, P.; Kitching, J. Subpicotesla atomic magnetometry with a microfabricated vapour cell. *Nature Photonics* **2007,** *1*, 649-652.

For Table of Contents Use Only

Metasurface-Integrated Photonic Platform for Versatile Free-Space Beam Projection with Polarization Control

Alexander Yulaev,[1,2] Wenqi Zhu,[1,2] Cheng Zhang,[1,2] Daron A. Westly,[1] Henri J. Lezec,[1] Amit Agrawal,[1,2] and Vladimir Aksyuk

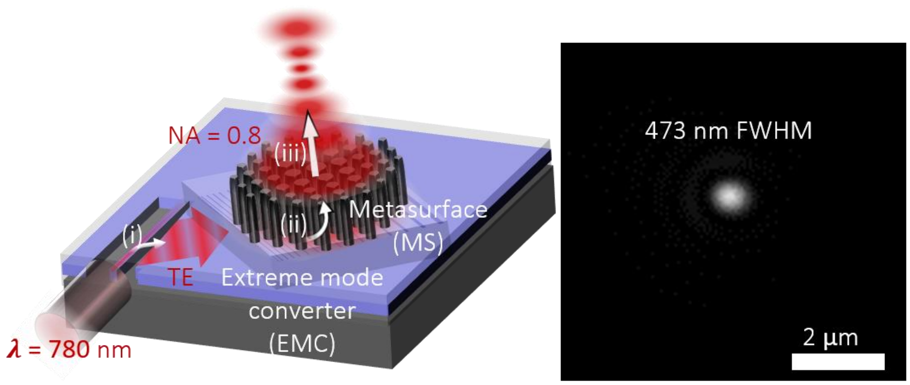

By integrating a dielectric metasurface with an extreme photonic mode converter, we create a versatile nanophotonic platform for efficient coupling to arbitrary-defined free-space radiation of 780 nm wavelength with well-controlled spatially-dependent polarization, phase, and intensity. The TOC depicts the schematic of our device and an optical micrograph of a diffraction limited focal spot.

Supporting information

Metasurface-Integrated Photonic Platform for Versatile Free-Space Beam Projection with Polarization Control

Alexander Yulaev,[1,2] Wenqi Zhu,[1,2] Cheng Zhang,[1,2] Daron A. Westly,[1] Henri J. Lezec,[1] Amit Agrawal,[1,2] and Vladimir Aksyuk[1,]*

[1]Physical Measurement Laboratory, National Institute of Standards and Technology, Gaithersburg, MD 20899, USA

[2]Maryland Nanocenter, University of Maryland, College Park, MD 20742 USA

7 pages

6 Figures

Characterization of a free-space beam emanated from an extreme mode converter (EMC):

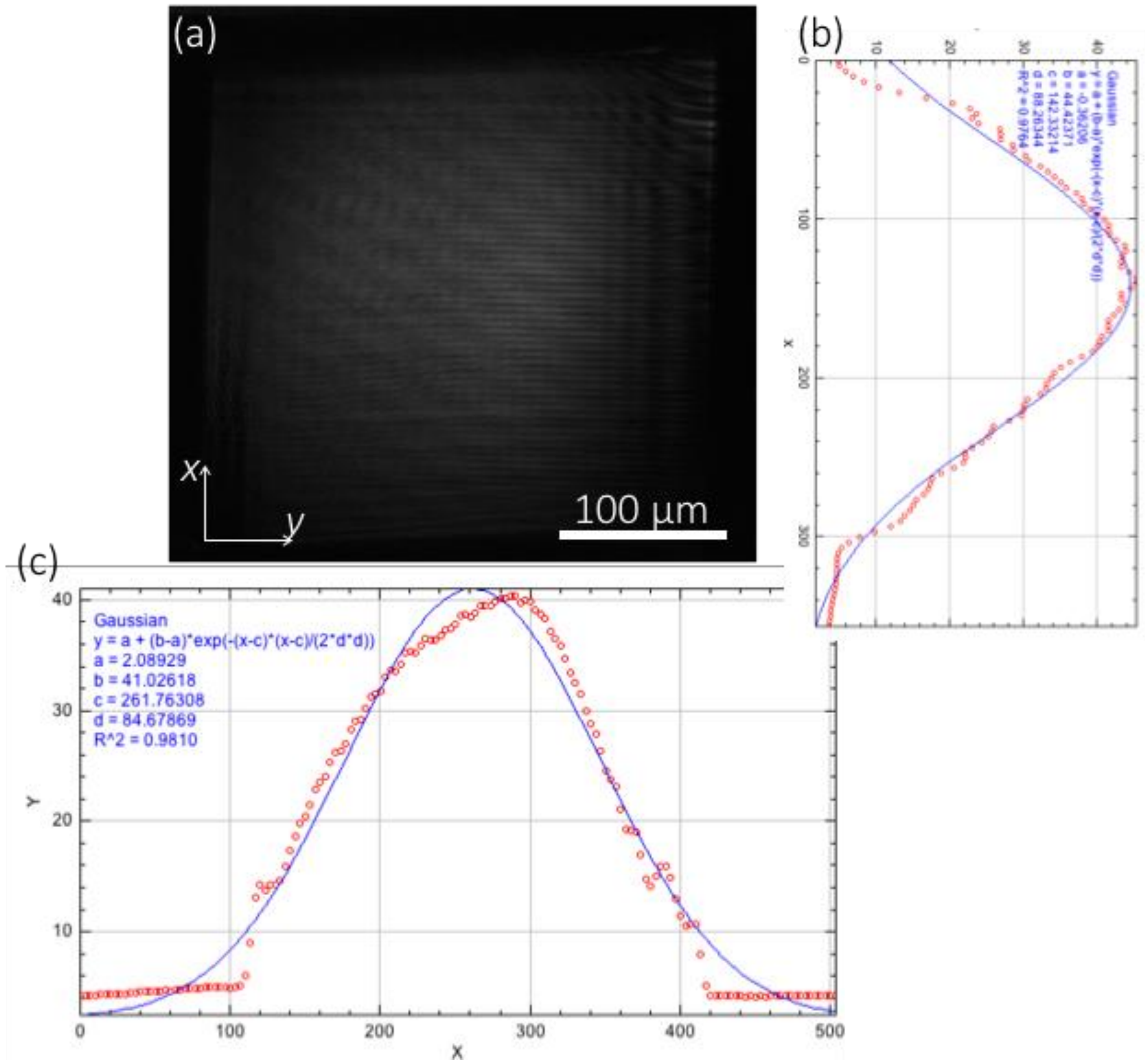

Fig. S1. Characterization of a free-space beam generated by an extreme mode converter. (a) A microscope micrograph of a free-space Gaussian beam projected by a 300 μm × 300 μm grating of an extreme mode converter. (b)-(c) Mode profiles along *x* and *y* axes obtained by integrating light intensity along *y* and *x* directions, respectively. Fitting the experimental profiles with a 1D Gaussian function reveals 208 μm and 199 μm full-width at half-maximum (FWHM) along the *x* and *y* axes, respectively.

Effect of metasurface (MS) phase compensation on a focal spot:

To analyze how the incorporated phase compensation affects the focal image, we fabricate and analyze an array of MS samples with a variety of angle correction values ranging from 0° to 6.5° in free space using Eq. (1) (Fig. S2). The left image in top row panel (a) shows the simulated E_x-field distribution after passing the 5° phase-compensated MS. The other images in Fig. S2 depict the experimental focal spots projected from several phase-compensated MSs assembled and precisely aligned on top of the EMC. The in-plane projection *x*' of the light beam direction is marked with a dashed white arrow in Fig. S2. When the phase compensation of the MS is not properly tuned for the incident beam angle, the focal spot distorts, appearing as a coma aberration. For a given photonic chip, only 4.3° phase-compensated MS results in an aberration-free focal spot image, which agrees well with the value of the beam tilt quantified from Fig. 3 b.

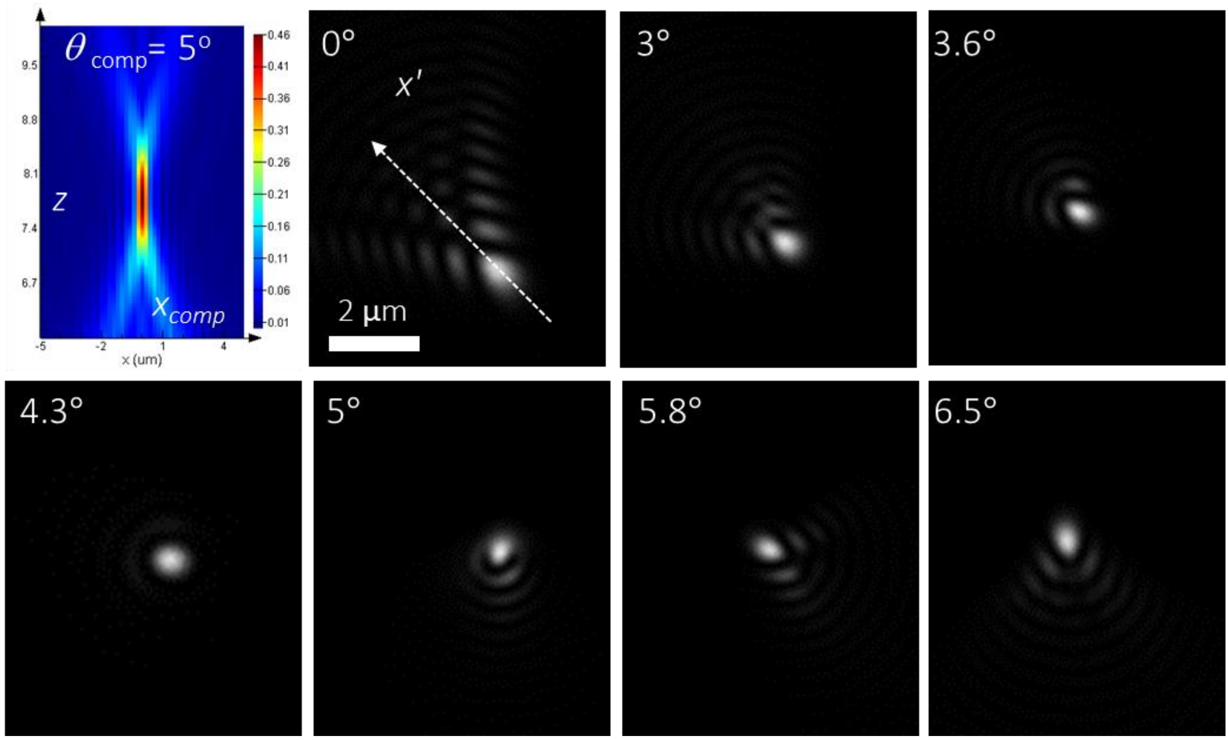

Fig. S2. Effect of phase compensation on focal spot aberration. The left image in top row is the longitudinal cross-section through a focused beam showing the simulated E_x-field distribution after passing 5° phase-compensated metalens along the x_{comp} direction. The other images acquired using 100× objective depict the experimental focal spots projected from 0° to 6.5° phase-compensated metalenses assembled and precisely aligned on top of the mode converter. The in-plane projection *x*' of the tilted incident light beam is marked with a dashed white arrow.

Effect of rotational misalignment on a focal spot:

An adjustable mechanical contact between the MS and the EMC allows for facile and precise alignment resulting in an aberration-free image of the focal spot. However, integrating photonic chips with other systems may require the monolithic fabrication or assembling of the MS and the mode expander into a single unit. Because the exact EMC beam direction may be affected by fabrication process variation, quantifying the engineering tolerance to rotational misalignments is of high importance. Fig. S3 illustrates how focal spots distort when the rotational misalignment between the MS and the photonic chip is introduced. The misalignment angle $\Delta\theta$ is defined between the in-plane projection x' of the collimated free-space beam and the direction of the 4.3° phase compensation x_{comp} (Fig. S2 a). Optical images of the focal spots with $\Delta\theta$ = -2.8°, 1.3° result in an axially symmetric non-distorted focal spot (Fig.S3 b and c). However, once the $\Delta\theta$ grows to ≈10°, the focal spot undergoes deformation with a clearly defined coma-shaped tail (Fig. S3 d). The orientation of coma aberration qualitatively coincides with an in-plane projection of the mismatch between the k-vectors related to a free-space beam and a phase-compensated direction. To sum up, the MS design is required for a specific incident k-vector to achieve clean and aberration-free focusing, however the focusing quality is tolerant to >3° azimuthal angle variation.

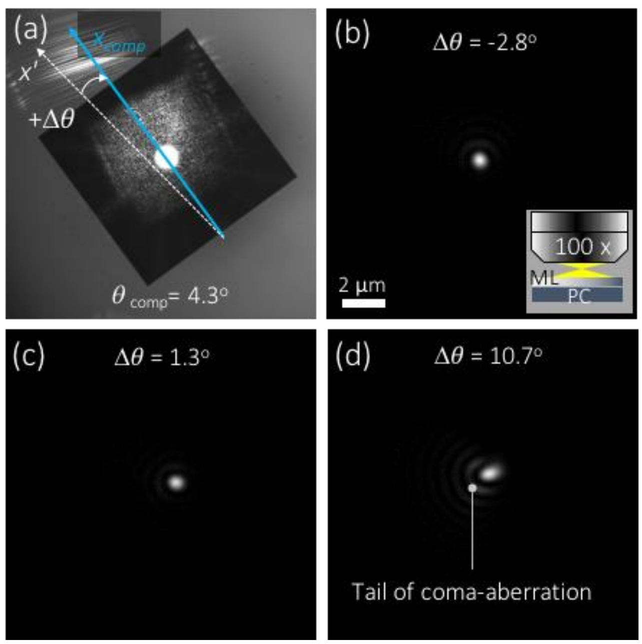

Fig. S3. Effect of rotational misalignment on focal spot aberration. (a) An optical image of the 4.3° angle compensated metalens stacked with the mode converter captured using a 10× objective. $\Delta\theta$ defines the rotational misalignment angle between the in-plane projection x' of the collimated free-space beam and the direction of the 4.3° phase compensation x_{comp} incorporated into the metalens design. (b)-(d) Optical images of the focal spots obtained using 100× objective from a 4.3° angle compensated metalens (NA = 0.8) for $\Delta\theta$ = -2.8°, 1.3°, and 10.7°.

FDTD simulations of high-NA focusing performed by a MS:

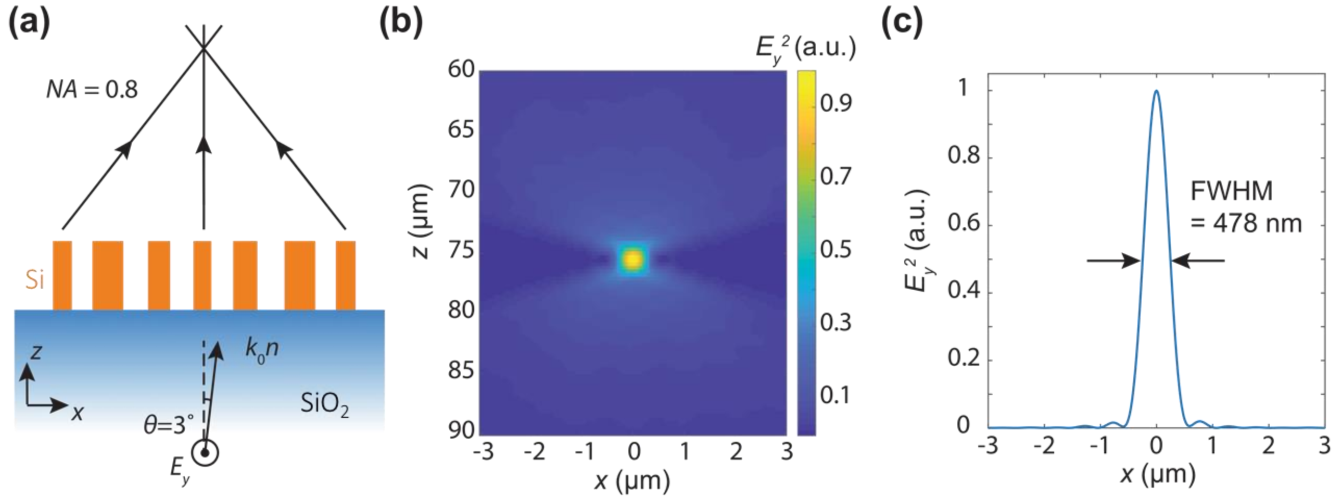

Fig. S4. Simulation of the metasurface that achieves focusing and tilt correction at the same time. (a) Schematic diagram of the metasurface functionality for an oblique angle of incidence $\boldsymbol{\theta = 3°}$ in a silica substrate. The incident beam has a Gaussian profile with a 195 μm FWHM. (b) The *xz*-plane cross section of the FDTD simulated $\boldsymbol{E_y}$ intensity at the vicinity of the focal spot. (c) Intensity profile of a focal spot along the *x*-axis. The simulated FWHM is 478 nm.

We use three-dimensional finite-difference time-domain (FDTD) simulations to validate the designing concept of the metasurface that achieves focusing and tilt correction at the same time. The nanopillar array that constitutes the metasurface spans 20 μm along the *x*-axis, where the in-plane dimensions are set to implement the phase function of a cylindrical lens:

$$\varphi(x) = \frac{2\pi}{\lambda_0}\left(f - \sqrt{x^2 + f^2}\right) - \frac{2\pi}{\lambda_0} n x \sin\theta \ ,$$

where $\lambda_0 = 780$ nm is the wavelength of incident light in free space, f is the targeted focal length of the metalens, n is the refractive index of the fused silica substrate, and θ is the angle of the obliquely incident light in the substrate. We have designed and simulated metalenses with targeted $f = 7.8$ μm (corresponding to NA $= 0.8$) for $\theta = 3°$ (Fig. S4 a-c). A diffraction-limited focal spot corresponding to the targeted numerical aperture and the desired tilt-correction is achieved (Fig. S4 c).

Characterization of a focal spot size:

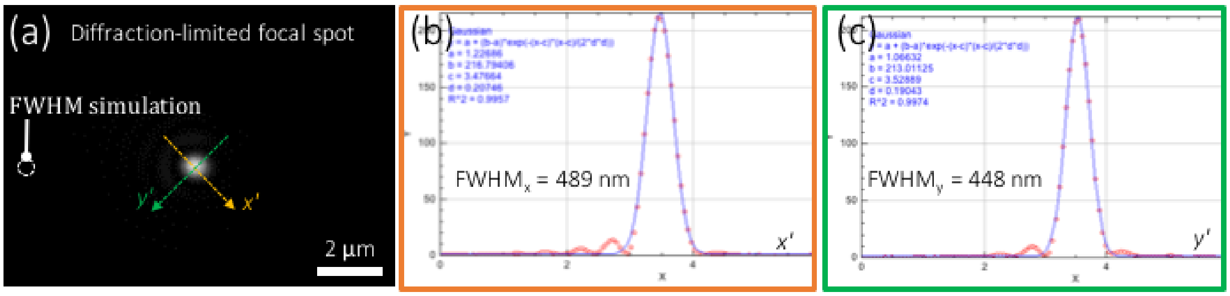

Fig. S5. Characterization of high-NA focusing of the photonic platform. (a) A focal spot pattern formed by 4.3° angle-compensated MS mounted on the EMC projecting ≈ 195 µm wide collimated Gaussian beam. The dashed circle indicates the FWHM of the diffraction-limited focal spot obtained using FDTD simulations. (b-c) Normalized intensity plot profiles (red circles) across the focal spot in panel (a) drawn along the *x*' and *y*' directions. The *x*' direction is collinear with the in-plane projection of the collimated free-space beam. Blue curves are Gaussian fittings.

FDTD simulations of the polarization conversion performed by a MS:

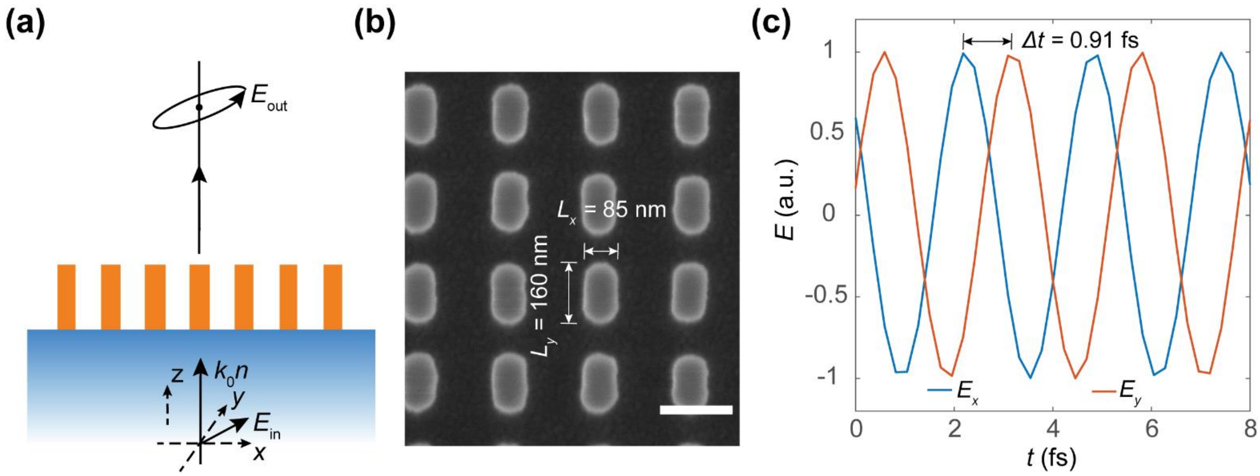

Fig. S6. Simulation of the polarization-conversion metasurface. (a) Schematic diagram of the metasurface functionality. (b) An SEM image of the fabricated metasurface characterized in Fig. 4. The in-plane dimensions, $L_x = 85$ nm and $L_y = 160$ nm, are measured for FDTD simulations. A scale bar represents 200 nm. (c) FDTD simulated $\boldsymbol{E_x}$ and $\boldsymbol{E_y}$ waveforms showing a time-delay of 0.91 fs.

The polarization conversion achieved in Fig. 4 is also confirmed by FDTD simulation. Here, the in-plane dimensions ($L_x = 85$ nm, $L_y = 160$ nm) and height ($H = 660$ nm) of the nanopillars are measured using scanning electron microscope (SEM) images. A linearly polarized light (electric field is 45° from the x-axis) is incident from the substrate side of the metasurface (Fig. S6 a). The simulated polarization state of the beam exiting the metasurface is shown in Fig. S6 c, with E_x delayed by $\Delta t = 0.91$ fs (corresponding to a phase delay of $\delta = 2\pi c\Delta t/\lambda_0 = 0.7\pi$) with respect to E_y, indicating an elliptically polarized light. The expected polarization contrast visibility is $e = 0.51$, closely matching the experimentally measured value of $e = 0.46 \pm 0.02$ in Fig. 4.